NUCL SCI TECH (2017) 28:78
DOI 10.1007/s41365-017-0228-5

Contrast sensitivity in 14 MeV fast neutron radiography

Chang-Bing Lu[1,2] · Jie Bao[1] · Ying Huang[3] · Peng Xu[2] · Xiong-Jun Chen[1] · Qi-Wei Zhang[1] · Xi-Chao Ruan[1]

Received: 19 April 2016 / Revised: 1 December 2016 / Accepted: 5 December 2016 / Published online: 28 April 2017

Abstract Fast neutron radiography (FNR) is an effective non-destructive testing technique. Due to the scattering effect and low detection efficiency, the detection limit of FNR under certain conditions cannot be determined. In order to obtain the minimum detectable thickness by FNR, we studied the contrast sensitivity of FNR lead samples, both theoretically and experimentally. We then clarified the relationship between pixel value and irradiation time, and sample materials and thickness. Our experiment, using a 4-cm-thick lead sample, verified our theoretical expression of FNR contrast sensitivity.

Keywords Fast neutron radiography · Contrast sensitivity · Experimental research

1 Introduction

Both fast neutron radiography (FNR) and thermal neutron radiography (TNR) are important non-destructive testing techniques [1–3]. These two methods have similar mechanisms and complementary effects; however, compared to TNR, the neutron in the FNR method has higher penetrability and can better detect light materials in thick heavy metals, which extends the application of neutron radiography. Presently, there exists a widely recognized international non-destructive testing standard, ASTME545-86, for TNR; however, no quantitative analytical standard has been established for the detection ability of FNR due to its scattering effect and low detection efficiency [4–6]. Generally speaking, the FNR technique is not as mature or developed as the TNR technique, which makes it crucial to develop new analysis approaches and criterion for FNR testing.

In recent years, international research has mainly focused on the construction and optimization of large-scale imaging systems [7–9], the development of conversion screens [10–12], parameter simulations [13–15], and preliminary applications [16–18]. In terms of spatial resolution, FNR uses the Klasens method to determine the modulation transfer function (MTF) of the system. In terms of contrast sensitivity, FNR uses tiered samples (made from the same materials, but with differing levels of thickness) for preliminary quantitative analysis [19–21]. Researchers have not yet solved an inherent problem in FNR's contrast sensitivity, i.e., the longitudinal detection limit of FNR when a fixed-thickness sample made from a certain material is irradiated by neutrons with the same energy and fixed intensity. As such, in this study, we conducted an experiment on the contrast sensitivity of 14 MeV FNR generated by the 600 kV Cockcroft–Walton accelerator in the Key Laboratory of Nuclear Data of the China Institute of Atomic Energy.

2 Modeling and analysis

The contrast sensitivity of an FNR system is defined as the minimum discernible variance in the thickness of a fixed-thickness sample along the incidence direction of the

✉ Jie Bao
2080917252@qq.com

[1] Key Laboratory of Nuclear Data, China Institute of Atomic Energy, Beijing 102413, China

[2] Xi'an Institute of High Technology, Xi'an 710025, China

[3] Science and Technology Information Center, China Academy of Engineering Physics, Mian-Yang 621999, China

detection beam. Contrast sensitivity serves as an index for judging a detection system's capacity for identifying the longitudinal thickness of a sample. If the thickness variance of a sample is less than the contrast sensitivity of the system, the sample is deemed undetectable. If the variance is equivalent to the contrast sensitivity, it is necessary to consider the comprehensive influence of irradiation time and scattering on the statistical fluctuation of the image contrast. Contrast sensitivity is primarily a TNR technical index, where its expression can be modified according to the characteristics of FNR applications.

Figure 1 shows the schematic of FNR data conversion. In Fig. 1, I_0 represents the intensity of incident collimated neutron beams, x is the thickness of the sample, I is the intensity of the neutron beam transmitted through the sample, the yellow rectangle represents a thin scintillator as a convertor, Q is the number intensity of fluorescence photons converted from the neutron beam by the convertor, and P stands for the pixel value of the image on the camera. When passing through the sample, the intensity of the neutron beam I has 2 parts: directly attenuated neutrons and scattered neutrons, where the latter depends on the geometry and material function of the sample. Therefore, I can be expressed as:

$$I = I_0 e^{-\mu x} + I_0 S(x, y, z, \mu_s), \tag{1}$$

where μ is the macroscopic cross section, μ_s is the material cross section, and $S(x, y, z, \mu_s)$ is the geometry and material function of the sample.

The fast neutrons continue to react with the converter. In the experiment, we used a thin BC400 plastic scintillator plate (consisting of carbon and hydrogen) as the convertor. The reactions between fast neutrons and carbon (or hydrogen nuclei) generate recoil nucleons and protons.

According to energy and momentum conservation principles, the equation of recoil nucleus energy E_A can be expressed as:

$$E_A = K_b E \cos^2 \theta, \tag{2}$$

where E represents the incident neutron energy, θ is the angle between the recoil nucleon and the incident neutron, A is the mass number of the recoil nucleon, and $K_b = \frac{4A}{(1+A)^2}$. E_A represents the energy of a recoil carbon nucleon if $A = 12$, and E_A is a recoil proton if $A = 1$. The ratio of K_b between a recoil carbon nucleon and a recoil proton is 1:3.57. Therefore, the energy of a recoil proton is much larger than that of a recoil carbon nucleon under the same initial conditions. Even for the same energy, a recoil proton generates more photon yield than a recoil carbon nucleon because of different reaction cross sections and ionization energy. Accordingly, the reaction of fast neutrons with a scintillator BC400 can be simplified as an interaction between neutrons and protons.

During the reaction process, the recoil protons impact the BC400 scintillator and generate fluorescence photons, whose intensity Q is:

$$Q \propto \varepsilon(E) I \sigma_{BC} m n, \tag{3}$$

where $\varepsilon(E)$ is the energy deposition function of the recoil proton energy (E) in the BC400 scintillator, σ_{BC} is the reaction cross section of the fast neutrons with hydrogen in the BC400 scintillator, m is the inherent nucleon density of the BC400 scintillator, n is the coefficient used to compensate for the recoil effect of carbon nucleons on photon intensity Q.

During the conversion process, we regarded each spot on the convertor that generated photons as a point of light source that illuminated at a full 4π solid angle. Blocked by the converter and influenced by the transmission path, the camera only recorded photons entering the camera lens at a very small solid angle. Ultimately, the fluorescence photons passed through the air, were reflected by the mirror and transmitted through the lens before being recorded by the CCD, which inevitably led to some attenuation. Considering all of these factors, we chose a parameter L to represent the equivalent distance from the light source to the camera and coefficients K_1, K_2 and K_3 to take into account airborne transmission efficiency, the reflection efficiency of the mirror and the transmittance capacity of the lens, respectively. The unit-time pixel value P/T detected by the CCD camera can be expressed as:

$$\frac{P}{T} = \frac{\vartheta(e) h v Q}{4\pi L^2} K_1 K_2 K_3, \tag{4}$$

where $\vartheta(e)$ represents a positive correlation function between the pixel value P and the photon energy e, h stands

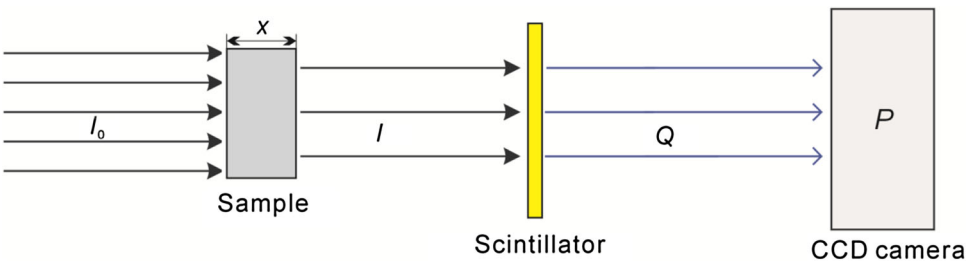

Fig. 1 Schematic of the data conversion of fast neutron radiography (FNR)

for the Planck constant, v stands for the photon frequency, and T is the irradiation time.

If the imaging system is free of stray light and the camera works stably under electrical refrigeration, the background image $B(w, v)$ with no neutron beam depends solely on the pixel coordinates w and v and is constant with respect to time. By combining Eqs. (2) and (4), the pixel value P is:

$$P = \lambda T I_0 e^{-\mu x} + \lambda T I_0 S(x, y, z, \mu_s) + B(w, v)T, \quad (5)$$

where $\lambda = \frac{\varepsilon(E)\vartheta(e)h\nu\sigma_{BC}mn}{4\pi L^2} K_1 K_2 K_3$ is a parameter related to the entire testing and imaging system.

In our experiment, we only considered variances in thickness Δx along the direction of the neutron beam. By differentiating both sides of Eq. (5), we obtained

$$\Delta P = -\mu\lambda T I_0 e^{-\mu x}\Delta x + \lambda T I_0 \dot{S}(x, y, z, \mu_s)\Delta x. \quad (6)$$

By setting ΔP as the minimum signal in the pixel value that can be detected by the computer system after digital statistics (which is related to the fluctuation of the system's counting statistics) we were able to calculate the minimum variance in thickness Δx as:

$$\Delta x = {}^{\Delta P}/_{\lambda T I_0 \left(\dot{S}(x, y, z, \mu_s) - \mu e^{-\mu x}\right)}. \quad (7)$$

If the scattering term $\dot{S}(x, y, z, \mu_s)$ had a minor effect on the pixel value, then we were able to simplify Eq. (7) as:

$$|\Delta x| \approx \left| {}^{\Delta P e^{\mu x}}/_{(\lambda T I_0 \mu)} \right|. \quad (8)$$

As shown in Eq. (8), when the influence of scattering could be ignored (i.e., if the scattering was too insignificant to be considered), the contrast sensitivity of the system [the minimum discernible thickness (Δx)] was inversely proportional to the irradiation time T, the macroscopic cross section μ of the sample and the intensity of the neutron source I_0. Moreover, it had a positive correlation to the minimum discernible signal of the pixel value ΔP.

3 Experimental study

Figure 2a depicts the schematic diagram of the relative positions of the sample and experimental facility. We generated a 14.1-MeV fast neutron source with a flux of $\sim 1.5 \times 10^{10}$ n/s and an energy of 14.1 MeV using a 600-kV high voltage multiplier. The neutron source emitted into the collimator from the large inlet at a 4π solid angle and incidents perpendicularly on the sample in a plane wave after passing through the collimator. We used a BC400 plastic scintillator plate with a size of 200 mm × 200 mm × 10 mm, a density of 1.032 g/cm^3 and an H:C ∼ 1.103:1 as the convertor. The collimator we used in the experiment was a composite structure consisting of lead, polyethylene, stainless steel and red copper. It had a length of $L = 147$ cm, with a maximum diameter at the outlet of $D = 8$ cm, and a minimum diameter inside of $d = 5.14$ cm. Based on the results of the experiment and the MC simulation, the flux ratios between the neutrons and the γ-ray near the collimator inlet (on the neutron source side) and the outlet were $\sim 1{:}2.81 \times 10^{-3}$ and $\sim 1{:}5.68 \times 10^{-4}$, respectively. The ratio between the neutrons and the γ-flux at the collimator outlet was approximately 25:1. Based on the experimental and simulation data, we determined that the X-ray and the γ-ray contribution to the dose rate on the BC400 scintillator was relatively low when compared to that of the neutrons. Furthermore, based on the simulation, the average conversion efficiency of the X-ray and the γ-ray with a 1 cm thickness on the BC400 scintillator was only 0.2%, whereas the neutron efficiency was approximately 2.2%, which was much higher than the gamma efficiency. The peak center of the BC400 scintillation light spectrum was located in the UV range (maximum wavelength 423 nm), which could barely be recorded by the CCD camera. In short, the experimental images' contribution to the pixel values from the X-ray and the γ-ray was relatively small compared to that of the neutrons.

The camera was a 1024 × 1024-pixel high-sensitivity scientific CCD. Each pixel corresponded to a 0.084 mm × 0.084 mm area on the converter. The sample was located 2 cm from the outlet of the collimator. The system collimation ratio was 294, and the geometric dullness of the system Ug was ∼0.0029 cm. We processed all of the images in the experiment after dark field deduction and flat field analysis had occurred. The testing times of the dark field and flat field were equivalent to the exposure time of the experiment images.

Based on the relationship between various parameters in the sample system and the pixel value of the image as stated in Eq. (5), we used two types of samples consisting of different materials and varied thickness. We then used different irradiation times for the two types of samples in the experiments. We chose lead and polyethylene as the materials for the two samples, because the former (lead) has a weak scattering effect of fast neutrons, while the scattering effect of the latter (polyethylene) is strong. Both samples were arranged in the shape of a triangular prism with a 5 cm × 10 cm × $5\sqrt{5}$ cm right triangle as the base, and a thickness of 5 cm, as shown in Fig. 2b, c, which also illustrate the direction of the transmitted neutrons.

Our analysis consisted of three steps: (1) first, we compared the influence of the different sample materials on the image pixel values; (2) second, we derived the relationship between the irradiation time and the image pixel values, and (3) third, we determined how the variations of sample thickness affected the pixel values for a certain material. Once we determined all three relationships, we

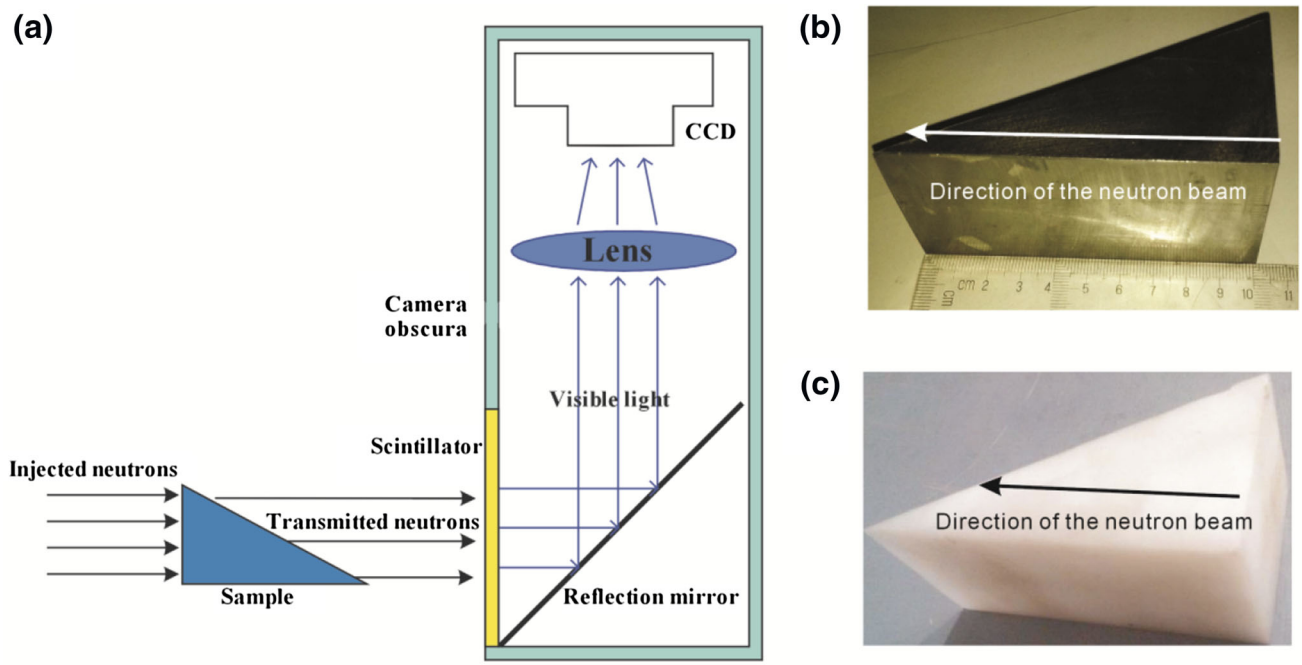

Fig. 2 Schematic diagram of the FNR experiment (**a**), a photograph of the lead sample (**b**), a photograph of the polyethylene sample (**c**)

were able to establish the corresponding discriminant of the system contrast sensitivity.

3.1 Experimental study on influential factors in pixel values

Figure 3a–c shows the fluorescence images of the lead sample's irradiation times at 1200 and 1800 s and the irradiation time of the polyethylene sample at 1800 s, respectively. The change of thickness in the images is presented in a horizontal direction. We subtracted the background of all of the fluorescence images to ensure equal irradiation times. We also filtered the medians before saving the data in ASCII format. Figure 3d–f shows the experimental data and fitting curves of the pixel values versus the sample thickness for the corresponding configurations. By visually comparing the images in Fig. 3a–c, one can see that Fig. 3c has the lightest coloring and superior grayscale layering, while Fig. 3a has the darkest coloring and poorest grayscale layering.

When analyzing the pixel values of the images, we chose a specific area marked as a rectangle with red edges, as shown in Fig. 3a–c. By averaging the pixel values along the width of the rectangle, we obtained the experimental data of the pixel values with respect to changes in thickness (along the length of the rectangular area) as shown in Fig. 3d–f.

In order to choose an appropriate function to fit the experiment data of pixel value, referred to Eq. (5), we eliminated the term $B(w,v)T$ as the background images which were already subtracted from the data, and ignored the term of scattering $S(x, y, z, \mu_s)$ for now since it did not have any explicit expression, and tried to conduct fitting with function $Y = KA\ e^{-\mu x}$ and evaluate the reliability of the fitted curve based on the goodness-of-fit R^2. In $Y = KA\ e^{-\mu x}$, Y, K, A, μ, x are related to the pixel value P, system parameter λ, neutron accumulation TI_0, material of the sample, thickness of the sample, respectively. The fitting functions of experimental data in the rectangular areas in Fig. 3a–c and the goodness-of-fit of each curve are shown in Table 1.

Judging by the goodness-of-fit data, the adoption of function $Y = KA\ e^{-\mu x}$ gives consistently high degrees of fitting, which indicates that choosing the exponential function Y as the fitting function is appropriate. However, compared with the lead sample of 1200-s irradiation time (a) and 1800-s irradiation time (b), the goodness-of-fit of the 1800-s-irradiation-time polyethylene sample (c) is the lowest. The reason might be that polyethylene has a stronger scattering effect of fast neutrons than the lead samples, where the scattering term $S(x, y, z, \mu_s)$ might have a relatively larger contribution to the pixel values of images and should be treated carefully rather than just ignored.

1200-s-irradiation-time (a) and 1800-s-irradiation-time (b) lead samples yield the same fitting value of μ (0.0131), while 1800-s-irradiation-time polyethylene gives a different μ value (0.0087), which demonstrates that parameter μ depends on the materials of the sample and is free of time. To consider the value of parameter KA, which should only depend on the system parameter λ, irradiation time T and

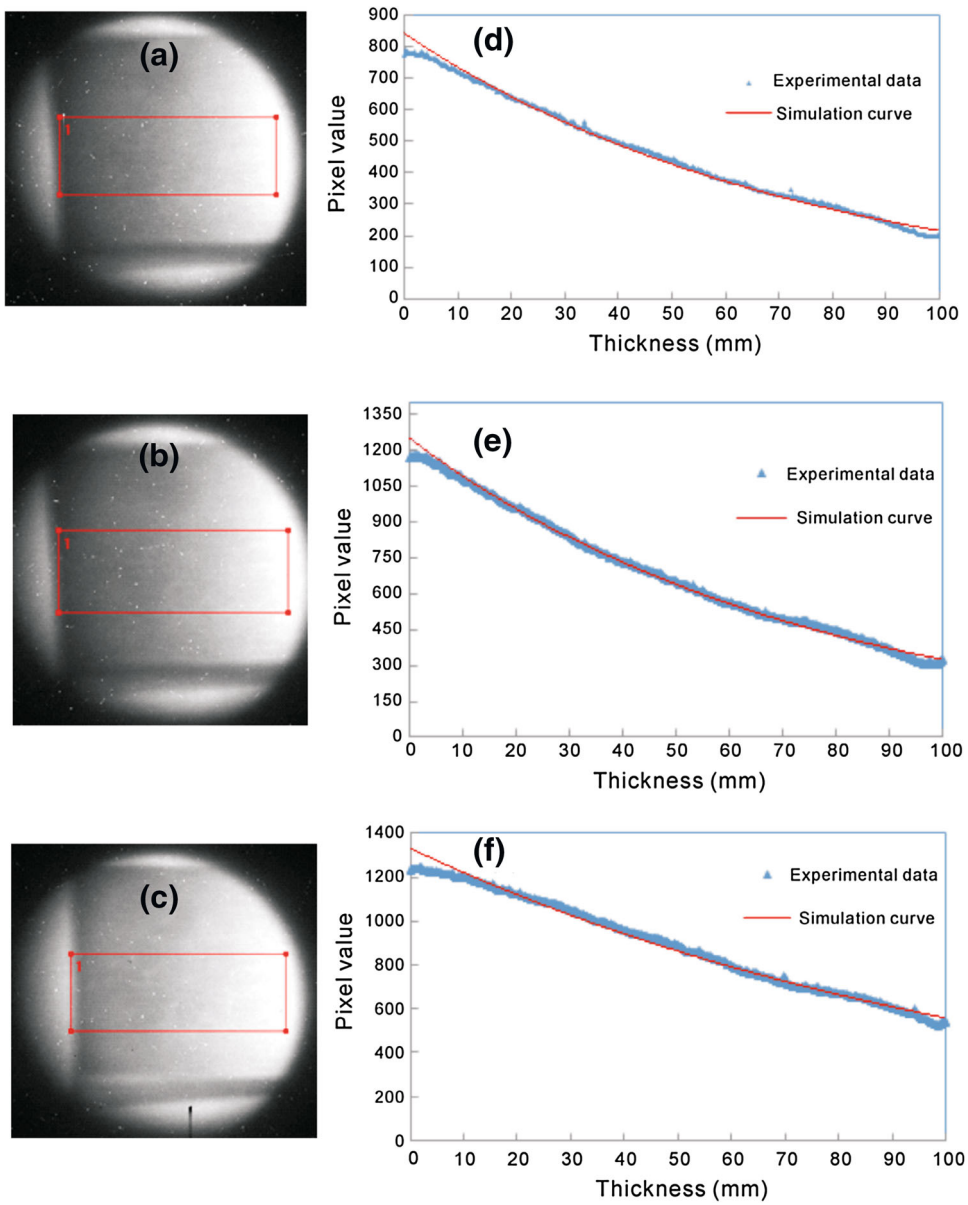

Fig. 3 Fluorescence images of the lead sample after 1200 s of irradiation (**a**) and 1800 s of irradiation (**b**), and a fluorescence image of the polyethylene sample after 1800 s of irradiation (**c**). The experimental data and simulation curves of the lead sample after 1200 s of irradiation (**d**) and 1800-s irradiation (**e**) and the experimental data and simulation curves of the polyethylene sample after 1800 s of irradiation (**f**)

Table 1 Fitting functions and goodness-of-fit for the experimental data in the rectangular areas depicted in Fig. 3a–c

Name	Sample	Fitting function	Goodness-of-fit
a	1200-s lead sample	$Y = 840.3130\ \mathrm{e}^{-0.0131x}$	$R^2 = 0.9925$
b	1800-s lead sample	$Y = 1211.3447\ \mathrm{e}^{-0.0131x}$	$R^2 = 0.9943$
c	1800-s polyethylene sample	$Y = 1330.3464\ \mathrm{e}^{-0.0087x}$	$R^2 = 0.9902$

neutron intensity I_0, if all the tests were achieved in one system with stable neutron sources and equivalent irradiation time, KA values should be the same for samples with different materials. However, the fitted data of 1800-s-irradiation-time lead sample (b) and 1800-s-irradiation-time polyethylene sample (c) give KA values as 1211.34 and 1330.34, respectively. The disparity in KA values of lead and polyethylene samples with equal irradiation time might further imply the influence of the scattering term $S(x, y, z, \mu_s)$ on the pixel values or might result from the drift of the neutron beam intensity I_0 for a relatively long time (thousands of seconds). Overall, for Fig. 3a–c, the pixel value undergoes a negative exponential function with respect to the thickness x approximately. These analyses show that $Y = KAe^{-\mu x}$ can basically satisfy the fitting of pixel value curves under certain limitations such as

scattering effect. The experiment results agree well with the theoretical derivation of pixel values.

3.2 Establishing the contrast sensitivity discriminants

The quantitative relations of pixel values to the irradiation time, sample thickness and materials of samples are used to set up the contrast sensitivity discrimination standard. After getting the function $Y = KAe^{-\mu x}$ of the pixel values followed by the change of thickness, the pixel value Y_0 at thickness X_0 can be calculated as

$$Y_0 = KAe^{-\mu X_0}. \tag{9}$$

According to the fluctuation theory of counting statistics, when the counting is Y_0, the range of the statistical fluctuation is:

$$Y_0 - \sqrt{Y_0} < \sigma_0 < Y_0 + \sqrt{Y_0}. \tag{10}$$

When the pixel value Y falls within the range of σ_0, it is deemed indistinguishable under condition Y_0; when Y is out of the range of σ_0, it is assumed to be distinguishable. Based on Eqs. (9) and (10), when the sample thickness is X_0 and irradiation intensity is A, we can calculate the minimum detectable concave depth of the sample X_c and the minimum detectable convex height X_v as follows:

$$X_c = X_0 - \frac{1}{\mu}\ln\frac{KA}{Y_0 + \sqrt{Y_0}}, \tag{11}$$

$$X_v = \frac{1}{\mu}\ln\frac{KA}{Y_0 - \sqrt{Y_0}} - X_0. \tag{12}$$

Equations (11) and (12) are the discriminants of FNR contrast sensitivity which can be used to determine the detection limit of FNR under irradiation of fast neutrons with specific energy, fixed intensity and for a sample of specific materials and thickness. The capability of an FNR system to identify material defects depends on its spatial resolution and capability to identify the variance of thickness in the longitudinal direction. Take groove defects for example, when the width of a groove is much larger than the spatial resolution of the imaging system, the system's capability to identify the groove should only depend on whether the depth of the groove is larger than the minimum discernible thickness, i.e., the contrast sensitivity of the system. Otherwise, the system's capability to identify defects will be affected by the system's spatial resolution on edge extension. Since the influence of spatial resolution is not considered in Eqs. (11) and (12) and the scattering term is ignored, Eqs. (11) and (12) are applicable only in the cases when the dimension of a defect is much larger than the system's spatial resolution, the edge broadening due to spatial resolution limit has less effect on the pixel values compared to that due to the sample thickness variation, and the effect of scattering is weak.

3.3 Experimental verification of the reliability of contrast sensitivity discriminants

In order to verify the reliability of the contrast sensitivity discriminants, we conducted an analysis based on the fitted curve $Y = 1211.3447\ \mathrm{e}^{-0.0131x}$ with high goodness-of-fit for the lead sample with an 1800-s irradiation time. When the sample's thickness X_0 was 40 mm, the corresponding pixel value Y_0 was 717.3 under the conditions of the experiment. Based on Eq. (10), pixel values fall into the range of 717.3 ± 26.8 and were considered undetectable. The minimum detectable concave depth X_c and convex height X_v were 2.8 and 2.9 mm, respectively, using Eqs. (11) and (12). Considering systematic errors, we aimed at the minimum discernible thickness of 3 mm for a 40-mm-thick lead sample in the FNR system.

For the experiment, we designed 2 cuboid lead samples with geometric proportions of 60 mm × 40 mm × 20 mm. One of the samples had 5 grooves with different depths on the 60 mm × 40 mm surface (as shown in Fig. 4a). The depth and width for each slot were the same: 1, 2, 3, 4 and 5 mm for the 5 grooves, respectively. During the experiment, the 2 samples were stacked to form a block measuring 60 mm × 40 mm × 40 mm. The experimental conditions included the neutron beam intensity and irradiation times being consistent with those in Eqs. (11) and (12). Figure 4b shows the fluorescence image of the lead sample in which the grooves (easily distinguishable by eye) have depths of 3, 4 and 5 mm, respectively.

We vertically added the pixel values in the red rectangle in Fig. 4b using the software *Andor Solis for Imaging*. We then plotted a statistical diagram of the pixel values in the horizontal axis, from which one can see 3 peaks which correspond to the groove depths of 3, 4 and 5 mm, respectively. Since the pixel values associated with the 1- and 2-mm-deep grooves were equivalent to the statistical fluctuations, they were undetectable. We only analyzed data from the central area of the images because they were more creditable than the areas near the boundary.

In conclusion, the minimum detectable thickness of the 40-mm-thick lead sample was $\sim$3 mm, which demonstrated the reliability of Eqs. (11) and (12). Moreover, the contrast sensitivity discriminant theory stated above was applicable for evaluating the minimum detectable thickness of a fix-thickness low-scattering sample in an FNR testing system. When applying such a method, attention must be paid to the applicable range and conditions of the criterion.

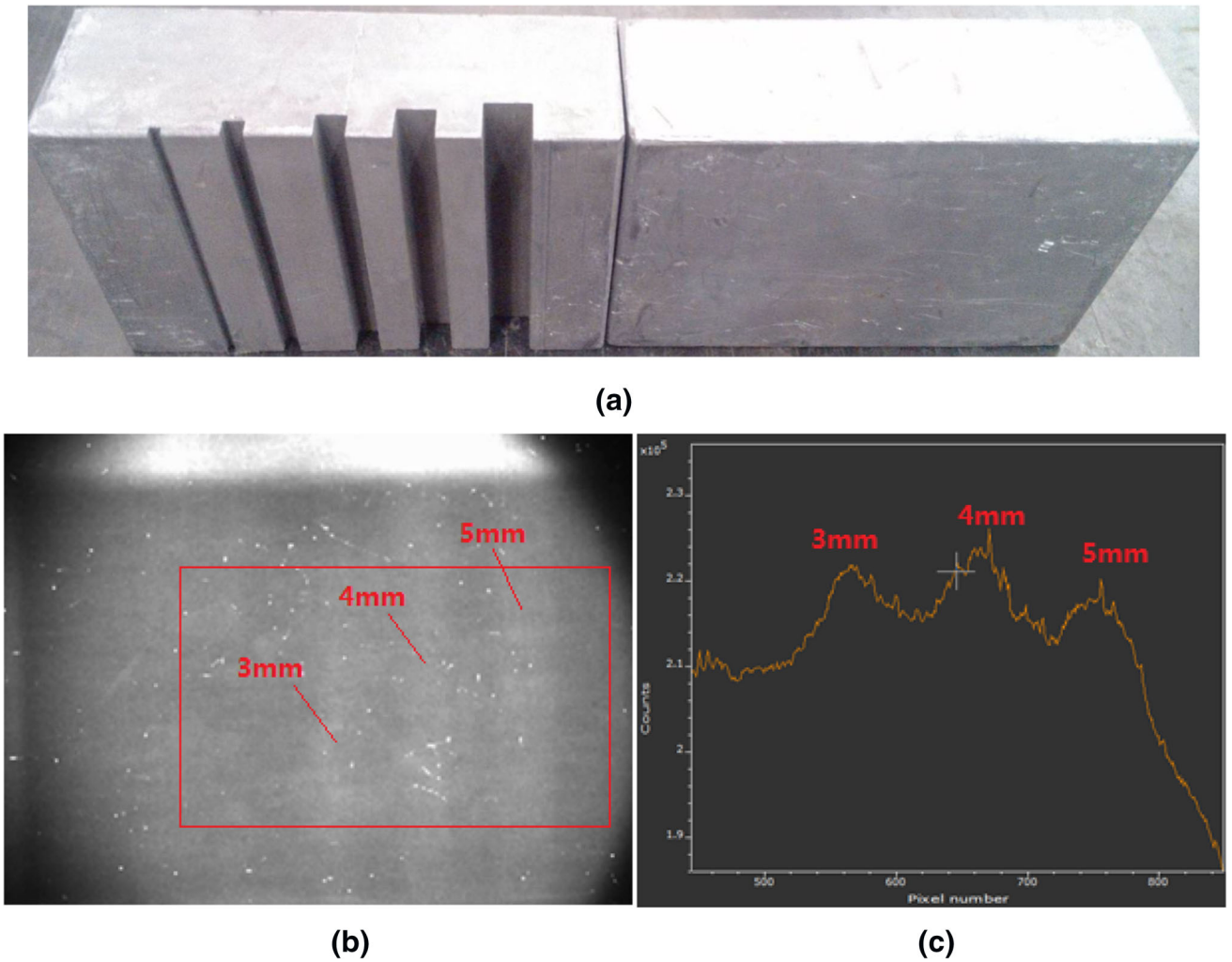

Fig. 4 A picture of the lead sample for verification of results (**a**); an image of the experimental verification results (**b**); and a statistical diagram of the pixel value data in the rectangular area (**c**)

4 Conclusion

We conducted a study on the contrast sensitivity of a 14-MeV FNR system using the 600-kV Cockcroft–Walton accelerator in the China Institute of Atomic Energy. We derived an equation for pixel values with respect to system sample parameters and irradiation time and determined the theoretical expression of contrast sensitivity. We selected lead and polyethylene samples to derive the relationship between pixel values and irradiation times, and sample materials and thickness. We then established the discriminants of contrast sensitivity and the reliability of the fitted curves. Afterward, we verified the discriminants using a 40-mm-thick lead sample.

Acknowledgements We would like to express our heartfelt gratitude to Professor Zhou Zu-Ying and Professor Tang Hong-Qing (of the China Institute of Atomic Energy) for their guidance. We would also like to thank the accelerator team for providing high-quality neutron beams.

References

1. M. Segawa, T. Kai, T. Sakai et al., Development of a high-speed camera system for neutron imaging at a pulsed neutron source. Nucl. Instrum. Methods A **697**, 77–83 (2013). doi:10.1016/j.nima.2012.08.079
2. B. Tang, C.G. Zhou, H.Y. Huo et al., The pilot experimental study of 14 MeV fast neutron digital radiography. Sci. China Ser. G **52**, 1090–1096 (2009). doi:10.1007/s11433-009-0184-0. **(in Chinese)**
3. S. Fujinei, K. Yoneda, K. Yoshii et al., Development of imaging techniques for fast neutron radiography in Japan. Nucl. Instrum. Methods A **424**, 190–199 (1999). doi:10.1016/S0168-9002(98)01326-6
4. H. Li, Y. Wu, C. Cao et al., Design optimization, manufacture and response measurements for fast-neutron radiography converters made of scintillator and wavelength-shifting fibers. Nucl.

Instrum. Methods A **762**, 64–69 (2014). doi:10.1016/j.nima.2014.05.079
5. Y.B. Zou, L.A. Guo, Z.Y. Guo et al., Development of a converter made of scintillator and wavelength-shifting fibers for fast neutron radiography. Nucl. Instrum. Methods A **651**, 62–66 (2011). doi:10.1016/j.nima.2009.01.130
6. R. Zboray, I. Mor, V. Dangendorf et al., High-frame rate imaging of two-phase flow in a thin rectangular channel using fast neutrons. Appl. Radiat. Isot. **90**, 122–131 (2014). doi:10.1016/j.apradiso.2014.03.023
7. B. Tang, Y. Wu, H. Li et al., The physics analysis and experiment study of zinc sulphide scintillator for fast neutron radiography. Nucl. Instrum. Methods A **729**, 327–333 (2013). doi:10.1016/j.nima.2013.07.063
8. H. Wang, V. Tang, M.J. Carrick et al., Reconstruction algorithm for point source neutron imaging through finite thickness scintillator. Nucl. Instrum. Methods A **693**, 294–301 (2012). doi:10.1016/j.nima.2012.07.018
9. S. Bishnoi, R.G. Thomas, P.S. Sarkar et al., Simulation study of fast neutron radiography using GEANT4. JINST **10**, P02002 (2015). doi:10.1088/1748-0221/10/02/P02002
10. P. Andersson, J.B. Valldor, E.S. Andersson et al., Design and initial 1 D radiography tests of the FANTOM mobile fast neutron radiography and tomography system. Nucl. Instrum. Methods A **756**, 82–93 (2014). doi:10.1016/j.nima.2014.04.052
11. J.M. Qi, F.Q. Zhang, J.C. Chen et al., Experimental research on light output characteristic of scintillator applied in pulsed y-ray and fast neutron imaging systems. At. Energy Sci. Technol. **48**, 715–720 (2014). doi:10.7538/yzk.2014.48.04.0715
12. C.B. Lu, P. Xu, J. Bao et al., Simulation analysis and experimental verification of fast neutron radiography. Acta. Phys. Sin. **64**, 198702 (2014). doi:10.7498/aps.64.198702. **(in Chinese)**
13. G. Nicholas, Y. Liu, R.Y. James et al., Development and commercialization of a fast-neutron/X-ray cargo scanner. Proc. Sci. Eng. **978**, 330–336 (2010)
14. H. Li, Y. Zou, S. Wang et al., Preliminary study on neutron radiography with several hundred keV fast neutrons. Chin. Phys. Lett. **29**, 1–4 (2012). doi:10.1088/0256-307X/29/11/118701
15. C.B. Lu, P. Xu, J. Bao et al., Preliminary experimental research of detail sensitivity in fast neutron radiography. Nucl. Technol. **38**, 080201 (2015). doi:10.11889/j.0253-3219.2015.hjs.38.080201. **(in Chinese)**
16. L.F. He, S.B. Han, H.L. Wang et al., Design of real-time neutron radiography at China advanced research reactor. Phys. Proc. **43**, 48–53 (2013)
17. I.S. Anderson, A.J. Hurd, R.L. McGreevy et al., *Neutron imaging and applications* (Springer, New York, 2009)
18. Z.Q. Cui, Z.J. Chen, X.F. Xie et al., Design of a magnetic shielding system for the time of flight enhanced diagnostics neutron spectrometer at experimental advanced superconducting Tokamak. Rev. Sci. Instrum. **85**, 11D829 (2014). doi:10.1063/1.4890536
19. L.F. He, S.B. Han, Y. Wang et al., Calculation and analysis of the neutron radiography spatial resolution. Nucl. Technol. **37**, 040502 (2014). **(in Chinese)**
20. X.H. Zheng, Y.B. Nie, X.C. Ruan et al., Experimental study of fast neutron radiography based on cockcroft walton generator. At. Energy Sci. Technol. **49**, 1117–1121 (2015). doi:10.7538/yzk.2015.49.06.1117
21. C. Cao, S. Wang, K. Tang et al., Comparison of two approaches to magnetic field quantification by polarized neutron images. Acta. Phys. Sin. **63**, 182801 (2014). doi:10.7498/aps.63.182801. **(in Chinese)**